Solid Freeform Fabrication 2024: Proceedings of the 35th Annual International
Solid Freeform Fabrication Symposium – An Additive Manufacturing Conference
Reviewed Paper

In-process Deformation Effect on Microstructure and Mechanical properties of Super Duplex Stainless Steel manufactured using Wire Direct Energy Deposition

P. Poulain[1*], J. Wang[1*], S. Williams[1], S. Bouvier[2], Y. Lu[1], N. Niknafsabrbekooh[1], S. Budnyk[3], A. Gavrilovic-Wohlmuther[3]

[1] Welding and Additive Manufacturing Centre, Cranfield University, Cranfield MK43 0AL, UK

[2] Université de technologie de Compiègne, Roberval (Mechanics, energy and electricity), Centre de recherche Royallieu - CS 60 319 - 60 203 Compiègne Cedex, France

[3] Schoeller-Bleckmann Nitec GmbH, 2630 Ternitz, Austria

[*] Corresponding authors (paul.poulain@cranfield.ac.uk, jun.wang.123@cranfield.ac.uk)

Abstract

Super Duplex Stainless Steels (SDSS) manufactured by Wire Direct Energy Deposition (WDED) often exhibit typical coarse columnar grain structures and undesirable phase balance, which is detrimental to mechanical performance and corrosion resistance. In this investigation, in-process mechanical works, including High-Pressure Rolling (HPR) and Machine Hammer Peening (MHP), were applied during the WDED process of SDSS to evaluate their influence on the microstructure and mechanical performance. Three single-pass walls were deposited using plasma transferred arc WDED process with different in-process conditions: no in-process deformation (as the control group); HPR with an average force of 75 kN; in-process MHP with a frequency of 36 Hz and energy per impact of 6 J. In-process mechanical work helps the transition from coarse columnar to fine equiaxed ferrite grains and also promote formation of austenite. These findings demonstrate the benefits of in-process mechanical work in the WDED process of SDSS.

1 Introduction

Super Duplex Stainless Steels (SDSS) are highly valued for their excellent combination of mechanical strength and corrosion resistance, making them ideal for demanding applications in the oil and gas, chemical, and marine industries [1]. The ferrite-austenite dual-phase microstructure of SDSS provides higher mechanical properties and better resistance to corrosion and cracking compared to other stainless steels [2]. Conventionally, SDSS components are manufactured using casting, forging, and machining, etc [3]. Nevertheless, the significant material wastage, extensive machining and more precise thermomechanical processing result in higher costs especially for complex geometries [4]. Therefore, it is imperative to develop alternative routes to manufacture SDSS structural components.

Additive manufacturing (AM) offers a promising alternative by enabling the fast production of intricate shapes with minimal material waste [4]. Among AM techniques, Wire Direct Energy Deposition (WDED) stands out due to its high deposition rates and cost-competitive for medium to large-scale components [5]. However, the WDED process for SDSS often results in coarse columnar grain structures and an undesirable phase balance, leading to anisotropy and compromised mechanical performance [6][7]. Recent advancements in the WDED process for SDSS have focused on addressing these microstructural challenges. Studies [8][9] have explored various approaches, such as optimising process parameters and incorporating post-deposition heat treatments, to improve the phase balance and refine the grain structure. A notable gap in the current research is the exploration of in-process mechanical

work to influence the microstructure during deposition. This technique has the potential to modify the grain structure and phase distribution without the need for additional post deposition heat treatment [10].

In this study, we investigate the impact of in-process mechanical work, specifically High-Machine Hammer Peening (MHP) and High Pressure Rolling (HPR), during the Plasma Transferred Arc (PTA) WDED process of SDSS. The aim is to evaluate how these mechanical works alter the microstructure, particularly the grain size and phase distribution. The findings from this research are expected to provide valuable insights into promoting the application of the WDED process where SDSS is essential for industrial production.

2 Experimental setup

2.1 Wire Direct Energy Deposition setup

The feedstock used in this study is a commercially available SDSS wire with a diameter of 1.2 mm. The deposition was performed on SDSS substrates with dimensions of 300 mm x100 mm x8 mm. The chemical composition of both the wire and the substrate are identical and can be found in Table 1. Chemical composition (wt.%) of the filler wires and substrate. Before deposition, the substrates were cleaned with acetone to remove any surface contamination.

Table 1. Chemical composition (wt.%) of the filler wires and substrate

Elements	C	Cr	Ni	Mo	Mn	Si	Cu	P
Filler wires & Substrate	0.017	29.9	6.57	2.18	0.95	0.36	0.14	0.018

Figure 1 shows the experimental setup for the PTA-WDED process. An EWM Tetrix 352 power source was used to provide the arc. An external wire feeder (Lincoln) was used to feed the SDSS wire into the melt pool. The motion of the torch is controlled by a 6-axis KUKA robot. A CMOS camera (Xiris XVC-1000) was used close to the torch to record the wire melting behaviour. The shielding gas used in this investigation is pure Argon. The key process parameters for deposition are listed in Table 2. The selection of these parameters is based on a certain preliminary process study to ensure that there will be no macro defects such as lack of fusion, humping, overflow, etc.

Table 2. Key process parameters for PTA deposition

Process parameters	Value
Current	210 A
Wire feed speed	2.25 m/min
Torch travel speed	2.67 m/min
Total layers	12 layers
Interlayer temperature	150°C
Contact to work distance	8 mm
Torch gas flowrate	0.8 L/min
Local shielding gas flowrate	80 L/min

Three single-pass walls were deposited using a back-and-forth deposition strategy with different in-process conditions, namely, as-deposit (control group), MHP, and HPR. In the deposition process of the MHP sample, when a layer is deposited, the hammerhead will be applied on top with a frequency of 36 Hz, an energy per blow of 6 J. In the deposition process of the HPR sample, one pass of cold rolling with an average force of 75 kN will be applied on top. Such deformation is repeated for each layer deposited until the completion of the deposition.

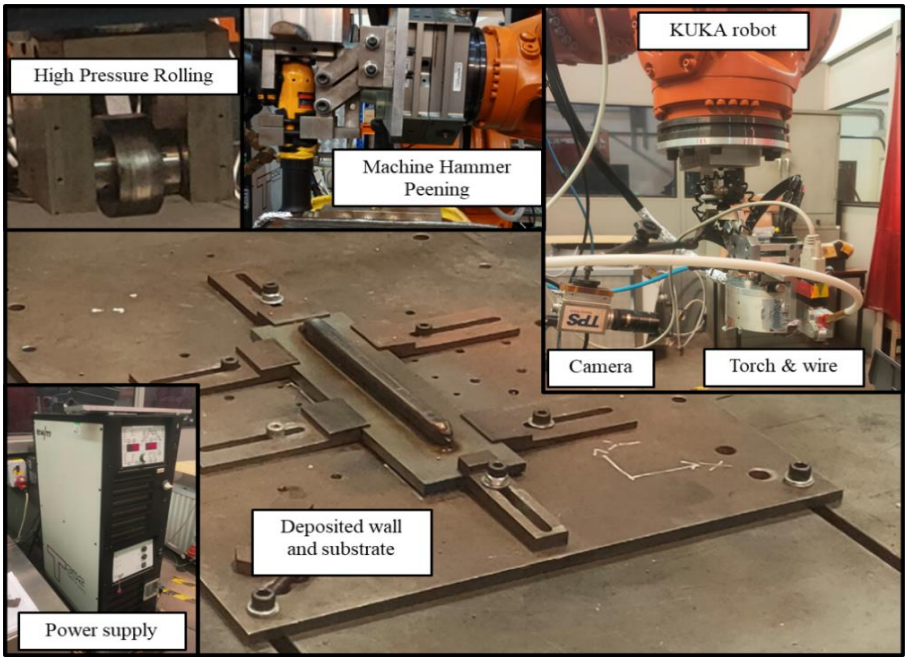

Figure 1. Schematic showing the experimental setup for the PTA Wire-DED process

2.2 Microstructural characterisation

Cross-section metallographic samples were extracted from the deposited structures, hot mounted, ground and polished in sequence. The samples were then electro-etched in a 40 wt.% NaOH solution using 3 V DC for 5 to 7 seconds until their surface turned straw yellow. Metallographic analysis was conducted using a Zeiss Stemi 508 for macro imaging. The fine microstructural features were characterised using a TESCAN S8000 scanning electron microscope (SEM) equipped with an Oxford Instruments' Symmetry EBSD detector with an accelerating voltage of 15 kV, a beam current of 15 nA and a step size of 1.6 µm. Microhardness tests were conducted using an Innovatest Falcon 503 hardness tester with a load of 0.5 kg over 10 s and a distance of 0.5 mm between indentations. The hardness maps were created by conducting three measurement lines in the cross-sectional plane of all samples with indentations spaced 0.5 mm apart. Each line was positioned 1 mm apart in the central part of the sample along the building height.

3 Results & Discussion

3.1 Macro morphology

The cross-sectional macro morphology of the three conditions, as-deposit, MHP, and HPR, are presented in Figure 2 a-c, respectively. All three walls are devoid of any shrinkage or

solidification defects (e.g. pores or cracks), indicating the feasibility and reliability of the PTA-WDED process and with in-process deformations. It also shows that increasing mechanical constraints resulted in a reduction in the total height. Specifically, the wall heights decreased from 25.2 mm to 24.7 mm and 22 mm for the as-deposit, MHP, and HPR samples, respectively, despite having the same number of layers. The wall width shows the contrary tendency.

In AM deposits, it is common to observe necking in the initial deposited layers [11]. However, the mechanical deformations induced by HPR effectively neutralized section reduction at the transition with the substrate. Besides, the plastic deformation is visible in the top layer: the in-process mechanical work flattens the top surface. The MHP process slightly flattens the top layer, while the HPR process leaves a flat surface approximately 7 mm wide. The as-deposit sample exhibits coarse columnar grains extending almost the entire height of the wall. The effect of MHP is most notable in the top region, which has not undergone reheating. The main bulk, which has undergone multiple thermal cycles, reverts to a columnar structure. This is not the case for the HPR sample. While almost columnar structures are visible on the lateral edges of the wall, the entire central band comprises a finer structure.

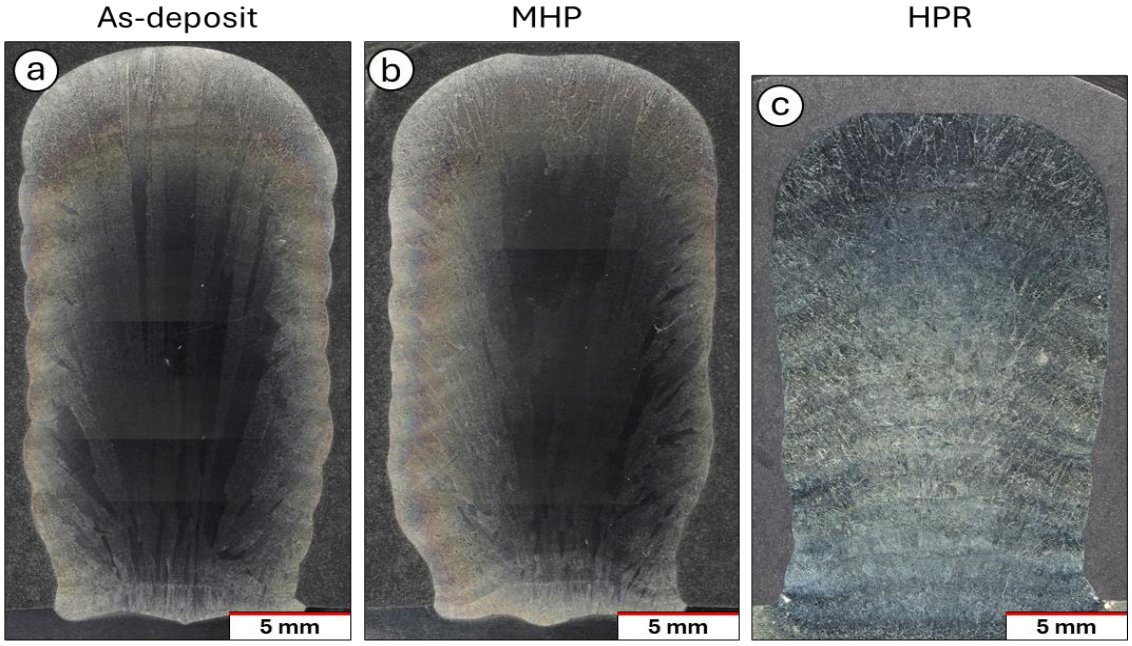

Figure 2. Macroscopic cross section view of PTA as-deposit (a), MHP (b) and HPR (c)

3.2 Grain morphology and orientation

To evaluate the influence of in-process mechanical work on the grain morphology and orientation of PTA-deposited SDSS, EBSD was performed on the cross-section plane (BD-building direction; ND-normal direction) covering the top surface of all three conditions. Figure 3 (a-c) present the inverse pole figure (IPF) maps at a lower magnification, illustrating the overall grain structure for each sample: as-deposit, MHP, and HPR. Figure 3 (d-f) show higher magnification IPF maps focusing on the central region of the walls, providing a detailed view of the grain structures.

Without applying in-process mechanical work (Figure 3a), extremely coarse columnar ferrite grains exceeding 10 mm in length with similar crystallographic orientations of (101) and (001) are revealed by the orientation map, indicating a preferential grain growth i.e., strong texture. This is the most effective path for thermal dissipation in cubic metallics [12], as the primary solidification driving force comes from the direction of the maximum temperature gradient [13]. Such pronounced orientation alignment leads to undesirable anisotropic behaviour, which can negatively affect the mechanical properties of the material in different directions. By applying MHP, a more deformed structure can be observed in its central region, directly beneath the impact zone (Figure 3b). However, columnar grains are still visible on the side and in the middle regions of the wall. The thermal cycles during deposition have promoted coarse and distorted grains, identifiable by variations in orientation within the grains and differing orientations compared to the control wall. The columnar grains in the lower region indicate that the thermal cycles have largely remelted the deformed structure, while induced some grain refinement and reorientation, suggesting a moderate texture with reduced anisotropy compared to the as-deposit sample. By applying HPR during deposition, the structure turns more homogeneous, featuring finer, equiaxed grains approximately 0.5 mm in size. There is no preferential grain orientation, and the crystallographic orientations are uniformly distributed, indicating a structure without texture. This homogeneity and isotropy are advantageous to overall mechanical properties, ensuring consistent distribution of stress and strain and reducing the likelihood of weak points.

The influence of in-process mechanical work on grain morphology and orientation could be explained by the correlation of hardening and remelting depth [14]. Recrystallisation is the main factor leading to grain refinement while the material must be hardened as a prerequisite for recrystallisation since the stored energy induced by deformation provides the thermodynamic driving force to trigger recrystallisation [15]. The key factor in triggering recrystallisation is heating the strained material to the recrystallisation temperature range without reaching the melting point [16]. Therefore, the relationship between the deformation-hardened depth and the remelting depth during the next deposition is crucial: the deformation-hardened depth must be greater than the remelting depth to ensure some strained material is heated to just below the liquidus temperature. If the remelting depth exceeds the deformation-hardened depth, all the strained material will melt, resulting in a solidified coarse columnar structure without any recrystallisation [14]. Obviously, in the MHP sample, the hardening zone is mostly remelted by the next layer deposition and the recrystallisation effect is very minimal. While in the HPR sample, the hardening depth is much larger than the remelting depth, leading to pronounced recrystallisation.

Figure 3 d-f show IPF maps at higher magnification focusing on the central region of the walls, providing a detailed view of the austenite grain structures. In the as-deposit sample (Figure 3d), the austenite grains are mostly found as very fine intragranular austenite needles inside the columnar ferrite grains. The banding phenomenon observed on the wide map is characterised by a slight increase in the austenite grains size forming these bands. In the MHP sample shown in Figure 3e, the intragranular austenite grains are larger, extending from the grain boundary austenite. This indicates that the MHP process promotes the growth and dispersion of austenite grains, although the lower regions still show the effects of the thermal cycles restoring the initial columnar structure. In the HPR sample (Figure 3f), as observed previously, the austenite grains agglomerate and nucleate from the ferrite grain boundaries. Moreover, intragranular austenite needles become coarser compared to as-deposit samples. The presence of Widmanstädter austenite can also be observed. The severe deformation induced by the cold rolling not only refined the ferrite grains but also enhanced the recrystallisation of

austenite grains. This results in a uniform and fine-grained structure, contributing to a more isotropic material with potentially superior mechanical properties.

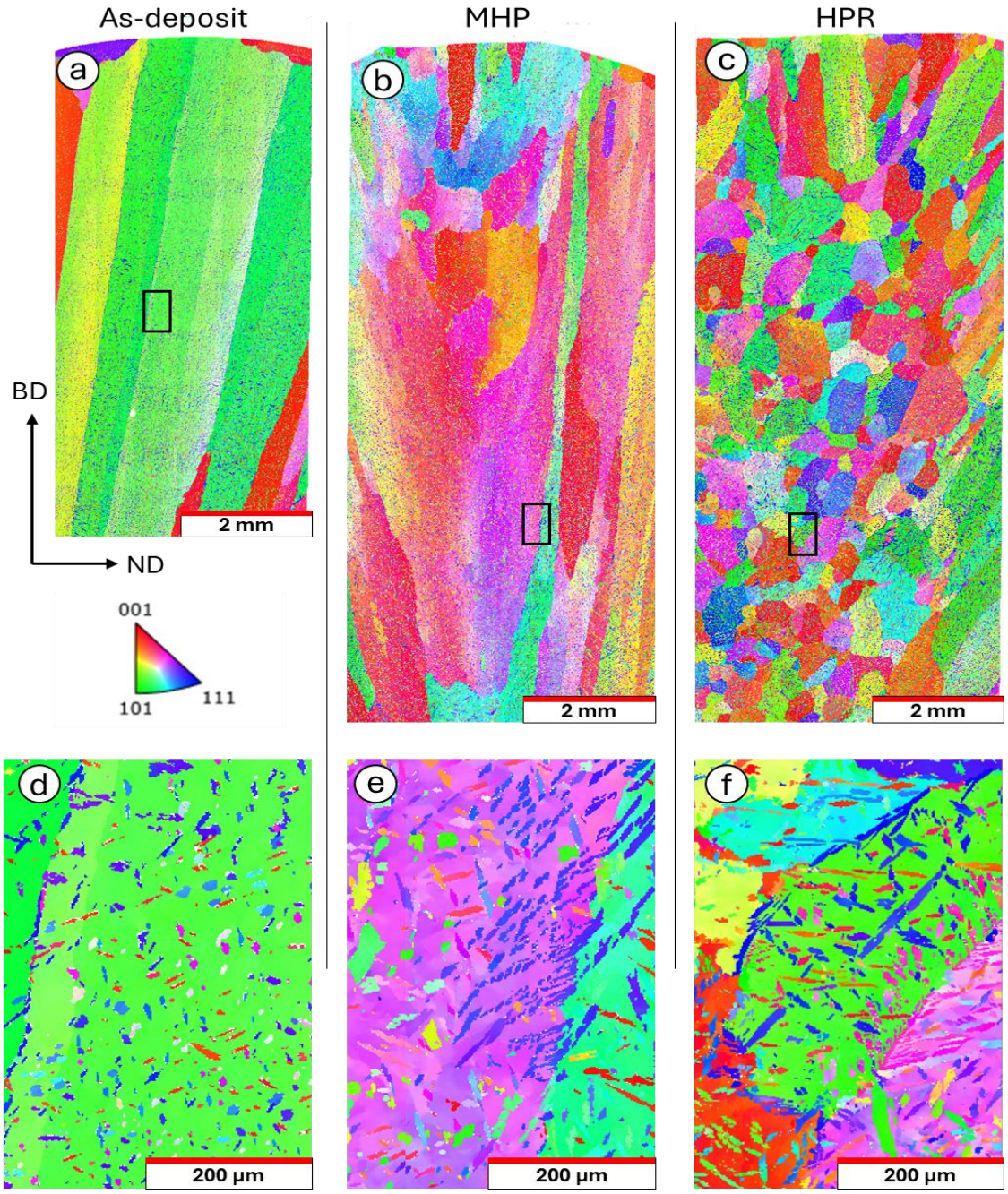

Figure 3. EBSD inverse pole figure orientation maps taken from the BD-ND plane of PTA as-deposit (a), MHP (b) and HPR (c); Higher magnification IPF maps on the central region of the walls of PTA as-deposit (d), MHP (e) and HPR (f).

3.3 Phase identification

Figure 4 shows the phase distribution maps obtained from EBSD analysis for the as-deposit, MHP, and HPR samples, respectively. In these maps, ferrite (BCC phase) is represented in red, while austenite (FCC) is represented in blue. Table 3 presents the volumetric phase balance in each condition.

The as-deposit sample (Figure 4a) exhibits a lower austenite content characterised by large columnar grains of ferrite. The austenite phase is primarily intergranular with a dimension of 20 µm, leading to an austenite percentage of 12.7%. This indicates a phase imbalance, which could contribute to undesirable anisotropic properties. In contrast, the sample subjected to MHP (Figure 4b) shows a noticeable increase in the austenite phase, reaching 20.8%. The mechanical deformation introduced by MHP appears to promote the formation of austenite at the grain boundaries of the fragmented ferrite grains. This increase in austenite content suggests that MHP can enhance phase balance by promoting the nucleation of austenite during the deformation process [17]. The samples treated with HPR (Figure 4c) displays an even higher austenite content of 23.8%. As mentioned previously the HPR process results in a homogeneous microstructure with fine equiaxed grains. This process effectively increases the volume fraction of austenite from the control sample.

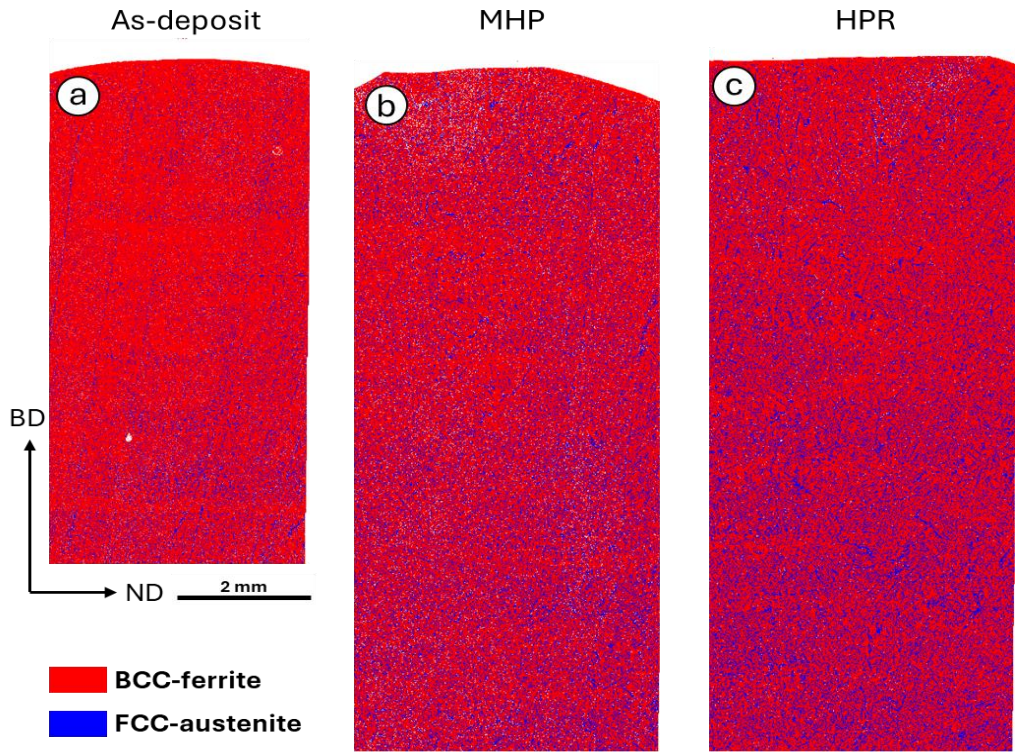

Figure 4. EBSD phase colouring maps of PTA as-deposit (a), MHP (b) and HPR (c)

Table 3. Phase distribution in SDSS samples with in-process mechanical treatments

Phase balance	As deposited	MHP	HRP
Ferrite phase [%]	87.3	79.2	76.2
Austenite phase [%]	12.7	20.8	23.8

3.4 Microhardness transition

The microhardness distribution maps under three conditions are presented in Figure 5 a-c and the comparison of the hardness transitions from top surface to bottom is shown in Figure 5d. The as-deposit sample demonstrates a uniform hardness distribution around 280 Hv0.5 throughout the cross-section. In contrast, the MHP sample exhibits a notable change in hardness distribution. The last 2.5 mm of the top region shows a significant increase in hardness, with a hardness value of over 350 Hv0.5. This region was subjected to mechanical peening after the final layer deposition. This localised increase in hardness suggests that the MHP process effectively induces work hardening in the upper layers by introducing dislocation. However, the decrease in hardness after 2.5mm shows that the reheating mechanism mitigates some of the hardening caused by cold work. A more pronounced hardening in the top region can be observed in the HPR sample, with a maximum value up to 370 Hv0.5. A gradual decrease in hardness till a steady state reaches 5 mm below the top surface can be observed. Additionally, a higher average hardness value of 300 Hv0.5 can be found in the HPR sample. This overall hardness enhancement can be attributed to the intense plastic deformation induced by the high-pressure rolling process, which results in significant work hardening and grain refinement. The comparison of the microhardness transition under three conditions highlights the effect of in-process mechanical deformation on basic material properties. The dislocation induced by in-process MHP is moderate and offset by the remelting of the next layer. However, the severe deformation induced by HPR leads to higher dislocation accumulation, leading to an increase in hardness of around 10%.

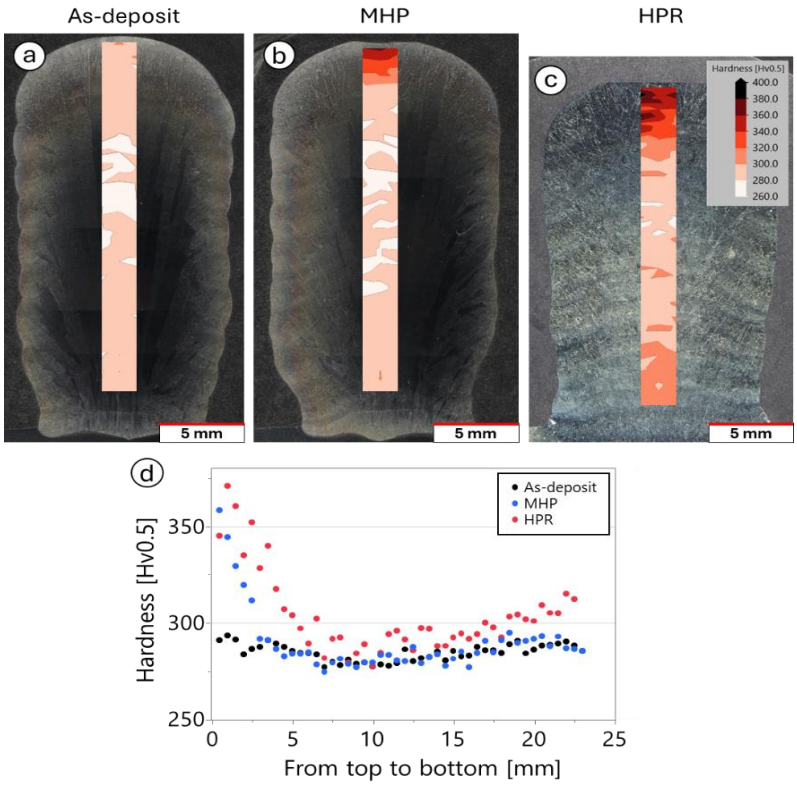

Figure 5. Microhardness maps overlayed on cross-sectional macro image of PTA as-deposit (a), MHP (b) and HPR (c); Microhardness profiles along the height of the samples (d). As-deposit in black, MHP in blue and HPR in red.

4 Conclusions

In this study, the impact of in-process mechanical work (MHP and HPR) on microstructure and mechanical performance of SDSS produced by the PTA-WDED process was analysed, and the major findings are summarised as follows:

- The introduction of in-process mechanical work significantly influenced the geometry of the walls, reducing overall height and increasing width, particularly under HPR conditions.
- In-process mechanical work leads to columnar ferrite grain fragmentation, and further deposition could trigger recrystallisation through reheating, promoting coarse columnar transfer into finer equiaxed grain structure.
- Noticeable increase in the austenitic phase volume fraction in in-process deformation samples, improving overall phase balance.
- Hardening induced by in-process mechanical work also results in an increase in hardness but will be offset to some degree by remelting during further deposition.

For the next step, studies on the influence of post-heat treatment on these three conditions and the relationship between in-process deformation and post-heat treatment will be explored to achieve an ideal phase balance (range of 40%-60%) and anisotropic microstructure.

Acknowledgements

The authors would like to thank Christof Group SBN for their financial support. The authors would also like to thank the entire technical team, especially Nisar Shah, Steve Pope, Tracey Roberts, and Kris Bramley for their assistance in the deposition process, metallographic and EBSD experiments.

References

[1] X. Zhang *et al.*, "Microstructure and mechanical properties of TOP-TIG-wire and arc additive manufactured super duplex stainless steel (ER2594)," *Materials Science and Engineering: A*, vol. 762, Aug. 2019, doi: 10.1016/j.msea.2019.138097.

[2] L. Sharma and K. Sharma, "Dissimilar welding of super duplex stainless steel (SDSS) and pipeline steel – A brief overview," *Mater Today Proc*, 2022, doi: 10.1016/j.matpr.2022.12.057.

[3] Y. Zhao, Y. Wang, S. Tang, W. Zhang, and Z. Liu, "Edge cracking prevention in 2507 super duplex stainless steel by twin-roll strip casting and its microstructure and properties," *J Mater Process Technol*, vol. 266, pp. 246–254, Apr. 2019, doi: 10.1016/j.jmatprotec.2018.11.010.

[4] S. W. Williams, F. Martina, A. C. Addison, J. Ding, G. Pardal, and P. Colegrove, "Wire + Arc additive manufacturing," *Materials Science and Technology (United Kingdom)*, vol. 32, no. 7, pp. 641–647, Jun. 2016, doi: 10.1179/1743284715Y.0000000073.

[5] S. C. A. Costello, C. R. Cunningham, F. Xu, A. Shokrani, V. Dhokia, and S. T. Newman, "The state-of-the-art of wire arc directed energy deposition (WA-DED) as an additive manufacturing process for large metallic component manufacture," *Int J Comput Integr Manuf*, vol. 36, no. 3, pp. 469–510, 2023, doi: 10.1080/0951192X.2022.2162597.

[6] S. Wu, Y. Zhang, M. Xue, and F. Cheng, “Grain refinement of flux-cored wire arc additively manufactured duplex stainless steel through in-situ alloying of Ti,” *Mater Charact*, vol. 209, Mar. 2024, doi: 10.1016/j.matchar.2024.113749.

[7] D. Zhang *et al.*, “Grain Refinement of Alloys in Fusion-Based Additive Manufacturing Processes,” *Metall Mater Trans A Phys Metall Mater Sci*, vol. 51, no. 9, pp. 4341–4359, Sep. 2020, doi: 10.1007/s11661-020-05880-4.

[8] R. Cervo, P. Ferro, and A. Tiziani, “Annealing temperature effects on super duplex stainless steel UNS s32750 welded joints. I: Microstructure and partitioning of elements,” in *Journal of Materials Science*, Aug. 2010, pp. 4369–4377. doi: 10.1007/s10853-010-4310-1.

[9] S. Saravanan, N. Sivagurumanikandan, and K. Raghukandan, “Effect of process parameters in microstructural and mechanical properties of Nd: YAG laser welded super duplex stainless steel,” in *Materials Today: Proceedings*, Elsevier Ltd, 2020, pp. 1248–1253. doi: 10.1016/j.matpr.2020.04.101.

[10] Y. Yang *et al.*, “Effect of a brief post-weld heat treatment on the microstructure evolution and pitting corrosion of laser beam welded UNS S31803 duplex stainless steel,” *Corros Sci*, vol. 65, pp. 472–480, Dec. 2012, doi: 10.1016/j.corsci.2012.08.054.

[11] A. Ty, Y. Balcaen, M. Mokhtari, and J. Alexis, “Influence of deposit and process parameters on microstructure and mechanical properties of Ti6Al4V obtained by DED-W (PAW),” *Journal of Materials Research and Technology*, vol. 18, pp. 2853–2869, May 2022, doi: 10.1016/j.jmrt.2022.03.169.

[12] Z. Lyu, Y. S. Sato, S. Tokita, Y. Zhao, J. Jia, and A. Wu, “Microstructural evolution in a thin wall of 2Cr13 martensitic stainless steel during wire arc additive manufacturing,” *Mater Charact*, vol. 182, Dec. 2021, doi: 10.1016/j.matchar.2021.111520.

[13] J. Wang *et al.*, “Evolution of crystallographic orientation, precipitation, phase transformation and mechanical properties realized by enhancing deposition current for dual-wire arc additive manufactured Ni-rich NiTi alloy,” *Addit Manuf*, vol. 34, Aug. 2020, doi: 10.1016/j.addma.2020.101240.

[14] X. Xu, S. Ganguly, J. Ding, C. E. Seow, and S. Williams, “Enhancing mechanical properties of wire + arc additively manufactured INCONEL 718 superalloy through in-process thermomechanical processing,” *Mater Des*, vol. 160, pp. 1042–1051, Dec. 2018, doi: 10.1016/j.matdes.2018.10.038.

[15] F. Martina, P. A. Colegrove, S. W. Williams, and J. Meyer, “Microstructure of Interpass Rolled Wire + Arc Additive Manufacturing Ti-6Al-4V Components,” *Metall Mater Trans A Phys Metall Mater Sci*, vol. 46, no. 12, pp. 6103–6118, Oct. 2015, doi: 10.1007/s11661-015-3172-1.

[16] J. Donoghue, A. A. Antonysamy, F. Martina, P. A. Colegrove, S. W. Williams, and P. B. Prangnell, “The effectiveness of combining rolling deformation with Wire-Arc Additive Manufacture on β-grain refinement and texture modification in Ti-6Al-4V,” *Mater Charact*, vol. 114, pp. 103–114, Apr. 2016, doi: 10.1016/j.matchar.2016.02.001.

[17] R. Strubbia, S. Hereñú, G. Gómez-Rosas, V. Fuster, and C. Rubio González, “Fatigue Life Improvement in Lean Duplex Stainless Steel by Peening Treatments,” *Metall Mater Trans A Phys Metall Mater Sci*, vol. 50, no. 12, pp. 5614–5626, Dec. 2019, doi: 10.1007/s11661-019-05455-y.